

Impact of a MoS₂ monolayer on the nanoscale thermoelastic response of silicon heterostructures

Davide Soranzio,^{*,†} Denny Puntel,[‡] Manuel Tuniz,[‡] Paulina E. Majchrzak,[¶] Alessandra Milloch,^{§,||,⊥} Nicholas M. Olsen,[#] Wibke Bronsch,[@] Bjarke S. Jessen,[△] Danny Fainozzi,[@] Jacopo S. Pelli Cresi,[@] Dario De Angelis,[@] Laura Foglia,[@] Riccardo Mincigrucci,[@] Xiaoyang Zhu,[#] Cory R. Dean,[△] Søren Ulstrup,[¶] Francesco Banfi,[∇] Claudio Giannetti,^{§,||,††} Fulvio Parmigiani,^{@,‡,‡‡} Filippo Bencivenga,[@] and Federico Cilento^{*,@}

[†]*Institute for Quantum Electronics, Eidgenössische Technische Hochschule (ETH) Zürich, CH-8093 Zurich, Switzerland*

[‡]*Dipartimento di Fisica, Università degli Studi di Trieste, Italy*

[¶]*Department of Physics and Astronomy, Interdisciplinary Nanoscience Center (iNANO), Aarhus University, 8000 Aarhus C, Denmark*

[§]*Department of Mathematics and Physics, Università Cattolica del Sacro Cuore, IT-25133 Brescia, Italy*

^{||}*ILAMP (Interdisciplinary Laboratories for Advanced Materials Physics), Università Cattolica del Sacro Cuore, IT-25133 Brescia, Italy*

[⊥]*Department of Physics and Astronomy, KU Leuven, B-3001 Leuven, Belgium*

[#]*Department of Chemistry, Columbia University, New York, NY, USA*

[@]*Elettra - Sincrotrone Trieste S.C.p.A., Strada Statale 14, km 163.5, Trieste, Italy*

[△]*Department of Physics, Columbia University, New York, NY, USA*

[∇]*Université de Lyon, CNRS, Université Claude Bernard Lyon 1, Institut Lumière Matière, F-69622 Villeurbanne, France*

^{††}*CNR-INO (National Institute of Optics), via Branze 45, IT-25123 Brescia, Italy*

^{‡‡}*International Faculty, University of Cologne, Albertus-Magnus-Platz, 50923 Cologne, Germany*

E-mail: davideso@phys.ethz.ch; federico.cilento@elettra.eu

Abstract

Understanding the thermoelastic response of a nanostructure is crucial for the choice of materials and interfaces in electronic devices with improved and tailored transport properties, at the length scales of the present technology. Here we show how the deposition of a MoS₂ monolayer can strongly modify the nanoscale thermoelastic dynamics of silicon substrates close to their interface. We achieve this result by creating a transient grating with extreme ultraviolet light, using ultrashort free-electron laser pulses, whose ≈ 84 nm period is comparable to the size of elements typically used in nanodevices, such as electric contacts and nanowires. The thermoelastic response, featured by coherent acoustic waves and an incoherent relaxation, is tangibly modified by the presence of monolayer MoS₂. Namely, we observed a major reduction of the amplitude of the surface mode, which is almost suppressed, while the longitudinal mode is basically unperturbed, aside from a faster decay of the acoustic modulations. We interpret this behavior as a selective modification of the surface elasticity and we discuss the conditions to observe such effect, which might be of immediate relevance for the design of Si-based nanoscale devices.

Transition metal dichalcogenides (TMDs) are a class of materials composed of atomic layers held together by van der Waals interactions, much weaker than the intralayer covalent bonds, giving them a marked two-dimensional character. This feature allows to obtain controlled thicknesses down to the single layers, useful for tuning several physical properties, such as the electronic band gap, the vibrational levels and the excitons, and for their implementation in thin nanodevices, *e.g.*, transistors, photodetectors and electroluminescent devices¹⁻⁴. In this respect, a key point is the interaction between TMDs and substrates, which has been shown to critically impact the heterostructure properties. Hence, the choice of the substrate constitutes a fundamental aspect for the application of TMDs heterostructures in electronic circuits⁵⁻⁸. To design functional devices, the thermoelastic response of the structure, *i.e.*, how fast can heat be dissipated, together with its elastic properties, which are also relevant for technological applications^{9,10}, are fundamental aspects to be considered.

In this work, we focus on the dynamics

over the typical length-scales of components used in nanodevices, *e.g.*, electric contacts and nanowires^{11,12}. In particular, we study the nanoscale thermoelastic response of a TMD monolayer (ML) deposited on top of a silicon substrate. The selected TMD material is molybdenum disulfide (MoS₂), which presents an interlayer separation of 0.65 nm and a ≈ 1.9 eV direct band gap at the ML limit¹³. To investigate the thermoelastic dynamics, we used the transient grating (TG) technique¹⁴. Specifically, nanoscale TGs were generated on the sample using free electron laser (FEL) extreme-ultraviolet (EUV) femtosecond pulses, to attain a ≈ 84 nm grating period. We studied the TG dynamics in three systems: a blank Si membrane, a ML MoS₂ transferred on a Si membrane and a ML MoS₂ grown on a Si wafer. The results showed a marked difference in the surface thermoelastic response of Si when ML MoS₂ is added. While two acoustic modes, a superficial Rayleigh-like and a longitudinal, were detected for the blank membrane, the longitudinal mode dominates for the MoS₂-covered samples alongside with a faster decay of the modulations. We ascribe

this fact to the different atomic motion involved, which is elliptical and localized close to the interface for the surface mode and parallel to the interface for the longitudinal mode. Underneath the acoustic modulations, we observed a slower decay of the non-oscillating background, usually assigned to thermal transport¹⁵, for the heterostructures compared to the blank substrate.

Results and discussion

A schematic of the samples is shown in Fig. 1(a). A blank Si membrane was used as a reference (sample #1). On top of a nominally identical membrane, a large-area monolayer of MoS₂ was prepared using the gold tape method (sample #2)¹⁶. For comparison to the membrane systems, we also studied a CVD-grown ML MoS₂, deposited on a Si wafer (sample #3). More details regarding the sample preparation are reported in the Methods section.

The MoS₂ coverage was tested using micro-Raman, taking advantage of the relation between the frequencies of the MoS₂ E_{2g}^1 and A_{1g} near-zone-center phonon modes and number of layers¹. Sample scans are reported in Fig. 1(b), with the ML-covered regions from sample #2 and #3 showing a much smaller (≈ 19 cm⁻¹) frequency separation of the modes, when compared to a thick multilayer, bulk-like island found on the Si frame (≈ 25 cm⁻¹), which is consistent with the literature. A systematic characterization of the samples is reported in the Supplemental Material¹⁷. Using the bulk MoS₂ film island as a reference, we conclude that the values found for both sample #2 and #3 are compatible with a ML coverage.

Fig. 1(c) illustrates the EUV TG experimental geometry. Two symmetric pump beams with wavelength $\lambda_{pu} = 39.9$ nm and time duration < 100 fs cross at the sample with an angle $2\theta = 27.6^\circ$ leading to a TG with a peri-

odicity $\Pi = 2\pi/k_{TG} = 83.6$ nm, where $k_{TG} = 4\pi \sin(\theta)/\lambda_{pu}$ is the modulus of the TG vector. The probe beam was set at $\lambda_{pr} = 13.3$ nm. More details regarding the EUV TG setup are provided in the Methods section. All the measurements were performed in reflection geometry, in a high vacuum and at room temperature. The diffracted signal was recorded using a CCD camera.

Fig. 2(a) shows the time-resolved TG signal for the blank Si membrane (sample #1). Before the temporal overlap between pump and probe, occurring at $t=0$, no signal is detected, while for $t > 0$ a transient diffracted signal appears. It is featured by modulations on top of the decay of the average signal, which is typical for a thermoelastic response.

To analyze the TG signal, we model its time-resolved intensity using the expression¹⁵

$$I(t) = \theta(t) \cdot \left| A_{th} e^{-t/\tau_{th}} + \sum_{i=1}^n A_i e^{-t/\tau_i} \cos(2\pi f_i t + \phi_i) \right|^2 \quad (1)$$

where $\theta(t)$ is the Heaviside function, A_{th} and τ_{th} are the amplitude and decay time usually assigned to the thermal component, A_i , f_i , τ_i and ϕ_i are the amplitude, frequency, time decay constant and phase of the i -th mode. Two modes are sufficient to describe the TG signal from sample #1. In fact, the square in the formula leads, when expanded, to a series of exponentially-decaying terms oscillating at frequencies 0, f_1 , f_2 , $2f_1$, $2f_2$, $f_1 + f_2$ and $f_1 - f_2$. The non-null frequency contributions can be visualized by fitting the experimental data to Eq. 1 with the oscillatory amplitudes A_i set to zero and performing the discrete Fourier transform on the residual signal (inset of Fig. 2(a)). The result is consistent with two modes with overtones, corresponding to the sums and differences of two frequencies f_1 and f_2 , such that $f_1 \approx 102$ GHz, $f_2 \approx$

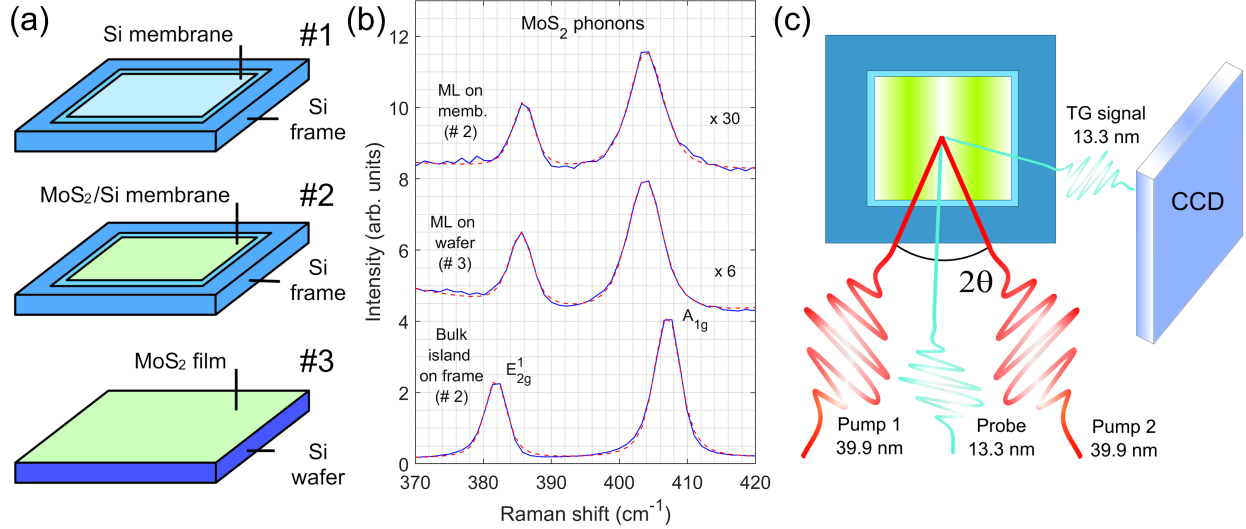


FIG. 1. (a) Samples studied during the TG experiments: #1 blank Si membrane, #2 MoS₂/Si membrane and #3 MoS₂/Si wafer. (b) Selected micro-Raman spectra showing the E_{2g}^1 and A_{1g} phonon peaks from the investigated samples: MoS₂/Si membrane, MoS₂/Si wafer and a MoS₂ bulk island. The Raman traces were rescaled and vertically shifted for clarity. The blue lines correspond to the experimental data, while the red-dotted ones to the best fit. (c) Scheme of the TG setup at the EIS-TIMER beamline at FERMI.

60 GHz, $2f_1 \approx 204$ GHz, $2f_2 \approx 120$ GHz, $f_1 + f_2 \approx 162$ GHz and $f_1 - f_2 \approx 42$ GHz, with the last one appearing as the left shoulder of the most prominent peak at $f_2 \approx 60$ GHz. By fitting the data using the full Eq. 1, we obtain the exact frequencies of the two modes, $f_1 = (105 \pm 1)$ GHz and $f_2 = (58.2 \pm 0.4)$ GHz. Moreover, the decay time is found to be $\tau_{th} = (39 \pm 2)$ ps.

We can rationalize the presence of these two modes as Lamb waves, namely, acoustic waves of the membrane^{18,19}. In TG experiments, their momentum is set by k_{TG} , while the propagation speed is related to the frequency-momentum dispersion relation of the material. Using the frequencies derived from the TG signal, it is possible to obtain the corresponding phase velocities with $v_{p,i} = f_i \Pi$. For sample #1, the detected modes correspond to $v_{p,1} = (8.81 \pm 0.09)$ km/s and $v_{p,2} = (4.87 \pm 0.03)$ km/s. These can be compared to the predicted phase velocity dispersion for the 200- μ m-thick Si membrane, through the

transverse resonance method^{18,20}, and using the longitudinal and shear velocities reported in Farnell and Adler²¹. The resulting phase velocities depend on the product $\rho = k_{TG}b$, where, in the present case, $k_{TG} = 0.075$ nm⁻¹ and $b = 200$ nm is the membrane thickness; hence $\rho \approx 15$. At this ρ value, two modes with phase velocities 8.89 km/s and 4.90 km/s, close to the longitudinal and transverse ones for Si, are predicted, compatible with the observed ones. The fitting procedure also provides the acoustic decay constants, which result $\tau_1 = (80 \pm 50)$ ps and $\tau_2 \approx 470$ ps. Both values are either comparable or larger than the investigated delay range, as shown in Fig. 2(a), hence a more accurate estimation would require further dedicated measurements.

Similar results have been previously reported for optical and EUV TG experiments in other materials for $\rho \gg 1$ ²²⁻²⁶. The acoustic modes are commonly identified as the ‘surface-skimming’ longitudinal wave (SSLW) and, in the limit of a semi-infinite substrate

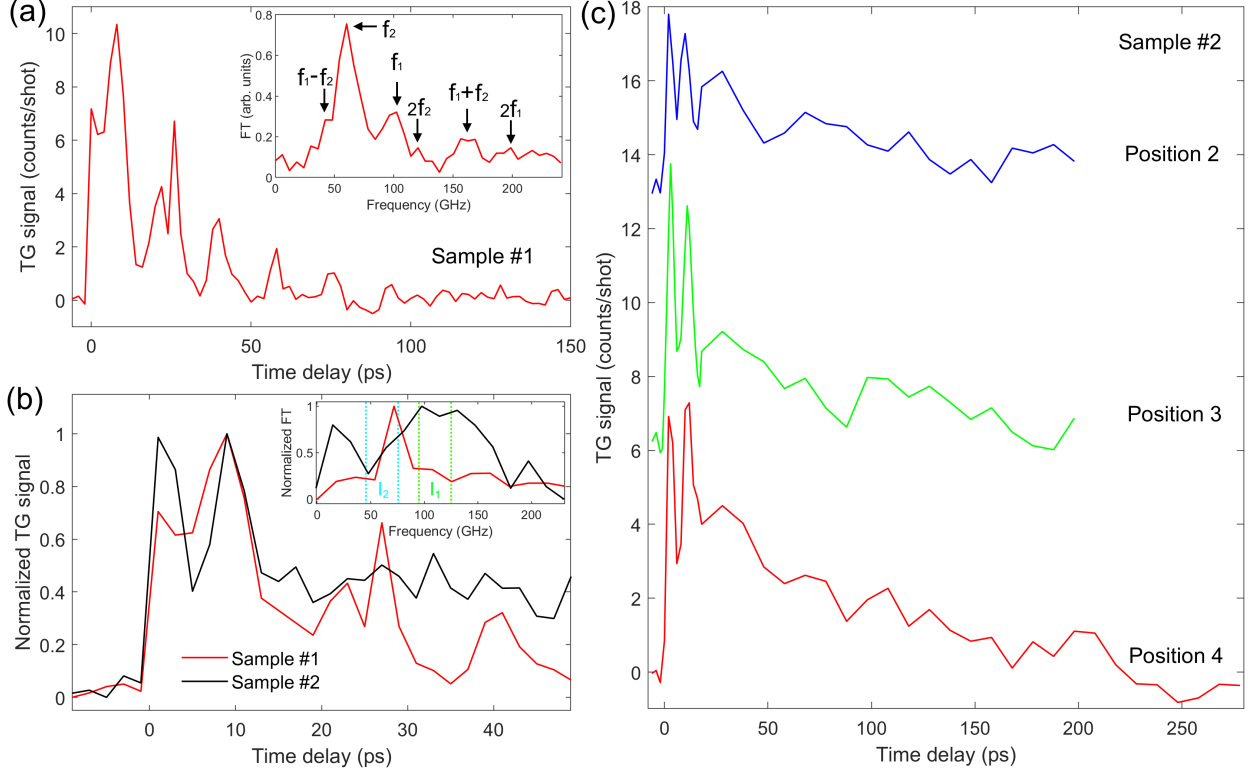


FIG. 2. (a) TG signal from the blank Si membrane (sample #1) at 0.34 mJ/cm^2 fluence; the inset shows the Fourier transform of the signal after the subtraction of an exponentially-decaying background for the ≈ 160 ps window. (b) TG signal from the MoS_2/Si membrane (sample #2) at 0.23 mJ/cm^2 fluence compared to the one from (a); the inset shows the Fourier transform of the two signals after the subtraction of an exponentially-decaying background for the ≈ 60 ps window; two integration region are marked (see text) (c) TG signal collected at different positions compared to (b) on the membrane of sample #2 under 0.25 mJ/cm^2 fluence.

($\rho \rightarrow \infty$), the Rayleigh surface acoustic wave (RSAW). As observed in our measurements, the SSLW at $f_1=105$ GHz is only visible in the first ≈ 15 ps in the TG signal, since it behaves like a leaky wave which rapidly decays in the bulk²². The RSAW decays on a longer timescale and involves elliptical displacements, *i.e.*, combined longitudinal and transversal motion. These are approximately localized at the surface within half a wavelength^{19,27}. A depiction of the two waves is given in Fig. 3, based on the derivation of their displacements with the method of potentials¹⁹; more details are provided in the

Supplementary Information¹⁷. The accurate prediction of the wave and heat propagation is complex and depends on many experimental details, such as the energy distribution in time and space. Nevertheless, in the reflection configuration used in the experiments, one expects the dominant contribution to the TG signal to arise from a coherent surface displacement, *i.e.*, from the RSAW^{22,28–30}.

In Fig. 2(b) we show the time-resolved TG signal for the MoS_2/Si membrane heterostructure (sample #2) compared to the blank membrane (sample #1). Differently from the blank case, here we observe an os-

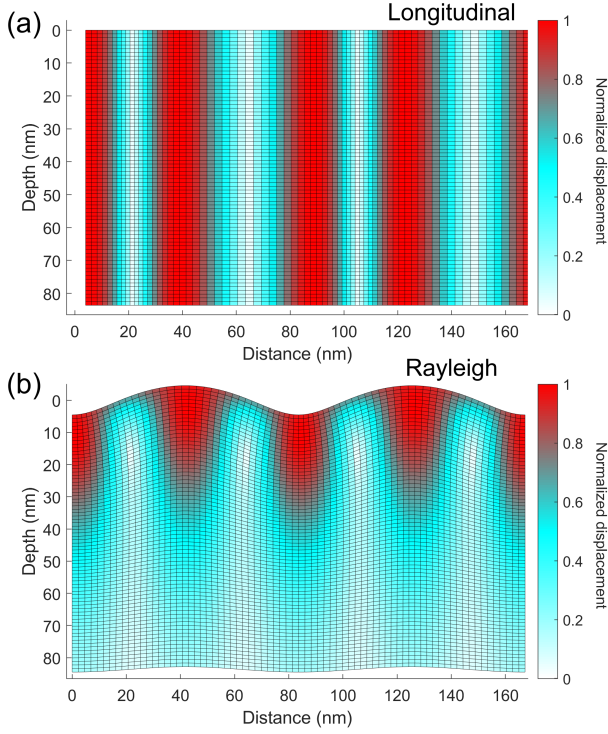


FIG. 3. Schematic representation of the displacements for the (a) longitudinal (b) Rayleigh acoustic waves in silicon. Their amplitude was arbitrarily set by a common factor to ease visualization; in the colorbar, the displacements were normalized to the maximum one with respect to the equilibrium positions.

cillatory signal in the first ≈ 15 ps only, with two prominent peaks. By performing the discrete Fourier transform after subtracting the non-oscillatory signal from the two traces as for panel (a), we observe a clear difference between sample #1 and sample #2 as shown in the inset in panel (b). In fact, if we integrate the spectral amplitude around the two main mode frequencies (f_1 , 90-120 GHz) and (f_2 , 45-75 GHz), we obtain that their ratio is $I_1/I_2 \approx 0.6$ for sample #1 and ≈ 1.9 for sample #2, pointing to a marked difference in the relative contribution of the two modes. Afterwards, the signal gradually decays with minor modulations on a longer timescale with

respect to the blank substrate (Fig. 2(a),(c)). Repeated scans at different sample positions gave an analogous response.

Fig. 4(a) shows a fluence dependence of the TG signal collected on the MoS₂/Si wafer (sample #3). Analogously to sample #2, we observe a response mainly localized in the first picoseconds with two main oscillation periods, resembling the SSLW detected in sample #1, followed by lower frequency modulations that emerge only for the highest investigated fluences, similar to the ones associated to the RSAW observed for sample #1. The TG signal acquired at different positions on the sample showed analogous features, albeit with some amplitude variability possibly connected to the local MoS₂ coverage (see Supplementary Information¹⁷). A comparison between the response of samples #2 and #3 under similar excitation conditions is reported in Fig. 4(b), showing similar features in the dynamics.

Considering the values of the attenuation length for Si and MoS₂, reported in the Methods section (at 39.9 nm, ≈ 237 nm and ≈ 40 nm respectively), it is evident that a MoS₂ ML cannot significantly alter the amount of energy deposited in the Si substrates. On the other hand, the monolayer/substrate interaction leads to a thermal resistance and changes in the dynamical heat distribution and elasticity at the interface of MoS₂/Si heterostructures; these properties are also influenced by the surface nanogroove of the substrate which is connected dynamically to the thermoelastic response^{31,32}. Therefore, one may expect surface modes like the RSAW, involving both longitudinal and transverse displacements¹⁹, to be more affected by the interaction with the MoS₂ ML rather than the longitudinal wave that leaks into the bulk. This reasoning is consistent with the experimental results reported in Figs. 2(b),(c) and 4(a), where a main oscillatory contribution with frequency close to the longitudinal mode dominates the TG signal of the samples #2 and #3, where

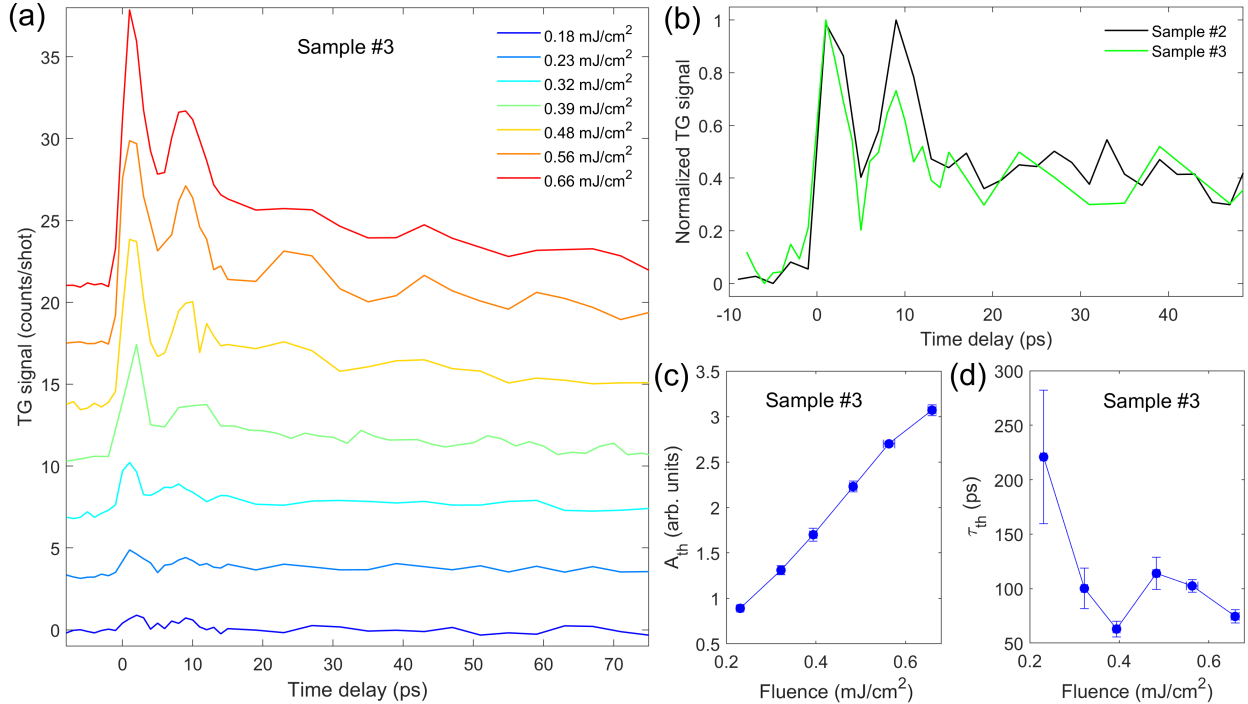


FIG. 4. TG signal from sample #3 (a) Fluence dependence of TG signal from sample #3. (b) Comparison between the normalized TG signals from sample #2 (0.23 mJ/cm^2) and sample #3 (0.25 mJ/cm^2). (c) Amplitude and (d) time decay constant of the non-oscillating component, as derived by the best fit of EUV TG waveforms from panel (a) to Eq. 1.

a ML MoS₂ is present.

To give a more quantitative view, we fitted the data from sample #2 and #3 using Eq. 1. Besides the TG signal collected from sample #3 at the highest fluences, the resolved oscillations are limited in time to about two periods of the longitudinal mode. This does not give enough data to effectively disentangle the contributions at distinct frequencies due to the correlation among the parameters, especially for the lower fluences. Nonetheless, it is possible to give good estimates keeping some of the parameters fixed. For sample #2, fixing the frequencies and phases of the two modes from the fit to the sample #1 TG signal (Fig. 2(a)), we obtained an average non-oscillating background decay constant $\tau_{th} = (170 \pm 10)$ ps over the different positions on the sample at 0.25 mJ/cm^2 (Fig. 2(c)). For sample #3, we first model the response at

0.56 mJ/cm^2 (Fig. 4(a)), where both modes emerge, keeping all the parameters free. The resulting frequencies are $f_1 = (113 \pm 5)$ GHz and $f_2 = (55 \pm 1)$ GHz, which are connected to the velocities $v_1 = (9.4 \pm 0.4)$ km/s and $v_2 = (4.62 \pm 0.09)$ km/s, close to the ones of the membrane. Regarding the decay constant of the acoustic modes, we obtained $\tau_1 = (5 \pm 1)$ ps and $\tau_2 = (70 \pm 40)$ ps. We then fix the frequencies, phases and time decay constants of the acoustic modes to extract the fluence dependence of the amplitude A_{th} and time decay constant τ_{th} , which we report in Fig. 4(c),(d). We omit the fit results for the lowest fluence as the time decay parameter is heavily influenced by the lower signal-to-noise ratio of this trace. While A_{th} increases linearly in the explored fluence range, τ_{th} settles around ≈ 100 ps for most of the explored range. The higher value $\tau_{th} = (220 \pm 60)$ ps from sample

#3 at 0.23 mJ/cm^2 may appear as an outlier, however it is compatible with the value derived from the sample #2 data under close excitation conditions ($\tau_{th} = (170 \pm 10) \text{ ps}$ at 0.25 mJ/cm^2).

To illustrate how the effects of the two acoustic modes combine differently between the blank Si membrane and the MoS₂ heterostructures, in Fig. 5 we present examples from the three samples: (a) #1 at 0.34 mJ/cm^2 , (b) #2 at 0.23 mJ/cm^2 and (c) #3 at 0.56 mJ/cm^2 . Here we remove from the fit (indicated with ‘Best fit’), obtained using Eq. 1, the contribution of one (‘Only SSLW’ or ‘Only RSAW’) or both (‘No osc.’) of the two acoustic modes, by setting their amplitude to zero. It is clear that the double-peak structure found in the MoS₂ heterostructures originates from the superposition between longitudinal and Rayleigh oscillations, where the relative height of the first two peaks is dictated by the combination of amplitude and phase of the two modes, more rapidly damped than the sample #1 case.

The observation of the influence from the ML MoS₂ on the TG signal is favoured by the choice of the substrate. We see from Fig. 4(a) that the amplitudes of the acoustic modes increase with the pump fluence, that determines larger displacements from the atomic equilibrium positions. The attenuation length of our pump beams is $\approx 237 \text{ nm}$, comparable to the membrane thickness $b \approx 200 \text{ nm}$ for sample #2. In another commonly employed substrate for TMDs such as sapphire, the attenuation length is just $\approx 13 \text{ nm}$, about 18 times smaller¹⁷. This gives a much higher excitation energy density than in the case of Si, potentially giving much larger displacements due to the RSAW mode, which are localized within a depth of half of the mode wavelength in the material (Fig. 3(b)). For fluences comparable to the ones employed for the data reported in Figs. 2 and 4, the RSAW in the TG signal dominates the response also in a

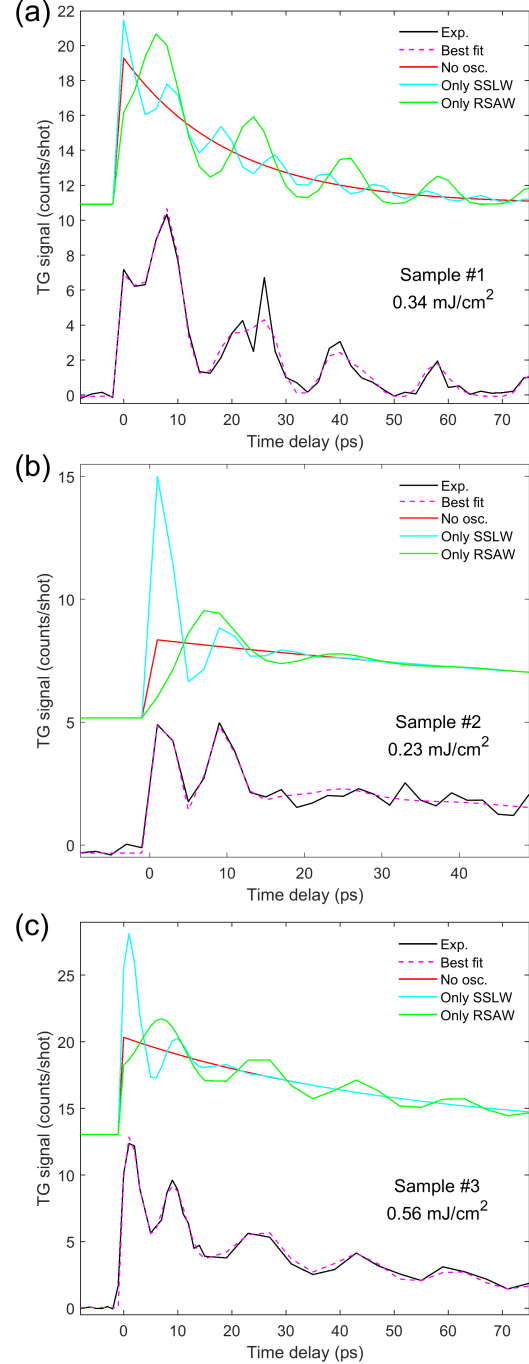


FIG. 5. Contribution of the acoustic modes to the TG signal illustrated by comparing the experimental data (Exp.) to the best-fit curve using Eq. 1 (Best fit) and by selectively removing their contribution from the fit result (only SSLW, only RSAW and no osc.) for samples (a) #1 (b) #2 (c) #3.

ML WS₂/Sapphire heterostructure. We provide an example of this in the Supplemental Material¹⁷.

Finally, we discuss the decay of the non-oscillatory component of the TG signal. On sample #1, we obtained $\tau_{th} = (39 \pm 2)$ ps. This value is substantially slower than what is expected by the standard thermal diffusive theory. Using the Si thermal diffusivity $\alpha_S \approx 0.055 \text{ } \mu\text{m}^2/\text{nS}$ from Johnson et al.³³ and our grating vector $k_{TG} = 0.075 \text{ nm}^{-1}$, the thermal diffusion theory predicts a decay $\tau_{Si} = 1/\alpha_S k_{TG}^2 \approx 3.2$ ps, about one order of magnitude smaller than the value from our experiment. This deviation was previously described as a consequence of ballistic transport, occurring for $k_{TG}\Lambda_{mfp} \gg 1$, where k_{TG} is the TG vector and $\Lambda_{mfp}=0.5\text{-}1 \text{ } \mu\text{m}$ is the median phonon mean free path^{33,34}.

With the addition of ML MoS₂, we observed a marked increase in the non-oscillatory time decay in samples #2 and #3. However, the decay constant found for the heterostructure is almost as large or higher than the investigated temporal windows for sample #2 and #3 (Fig. 2(b),(c) and 4(a)). Therefore, a further dedicated set of measurements is required for an accurate explanation of this result. Based on the considerations for Si, it might be important to take into consideration a model that includes non-diffusive thermal transport, the interfacial thermal resistance in the MoS₂ and Si layers^{5,32} and possibly the influence of charge recombination at the MoS₂/Si interface³⁵. Furthermore, as we have shown in our work, the amplitude and time decay of the oscillations of the acoustic modes are markedly affected by the deposition of ML MoS₂, suggesting a possibly less effective contribution to the thermal transport.

Conclusion

In this work we used nanoscale EUV transient gratings to comparatively study the nanoscale thermoelastic response of a thin Si membrane and a Si wafer, both covered with ML MoS₂, and of a blank, thin Si membrane. The results show how a monolayer of a TMD material, in our case MoS₂, can dramatically modify the response of the Si substrate close to its surface. In particular, ML MoS₂ leads to the almost complete suppression of the surface acoustic wave, which involves elliptical motion localized in proximity of the surface, for comparable excitation fluences. Differently, the longitudinal wave, which does not involve a motion perpendicular to the surface, appears to be less affected, albeit more quickly damped as well. The two Si substrates used, a membrane and a wafer, gave a qualitatively similar behavior. Finally, we observed a slower decay of the non-oscillatory response in the heterostructure, when compared to the blank substrate. This effect is possibly connected to the impact of such acoustic modes on the transport properties of the system at the nanoscale. This work extends the time-domain investigations of the role of Van der Waals materials on the acoustic response of heterostructures, beyond the case of coherently excited thin layer breathing modes investigated, *e.g.* by time-resolved Brillouin spectroscopy³⁶.

Methods

Samples

Our study focused on samples based on a 200-nm-thick, 1.6x1.6-mm²-large boron-doped Si membrane, commercially produced by Norcada³⁷, nominally having < 1 nm rms surface roughness on both front and back sides of the membrane, supported by a 200- μm -thick Si frame. The three samples are depicted in Fig.

1(a). One blank Si membrane was used as a reference (sample #1). On top of a nominally identical membrane from the same manufacturer, a large-area monolayer of MoS₂ was prepared using the gold tape method¹⁶ (sample #2) at Columbia University. Additionally, we studied a CVD-grown MoS₂ monolayer, deposited on a 0.52-mm-thick Si wafer, commercially available from SixCarbon Technology (sample #3).

Micro-Raman characterization

The uniformity and thickness of the MoS₂ films were tested with a micro-Raman Renishaw inVia instrument using a continuous-wave 532 nm laser at the I-LAMP laboratories in Brescia (Italy). Measurements were acquired under an incident power of 5 mW for the samples with a deposited MoS₂ monolayer and 0.5 mW for the blank substrates. At focus, under 100x magnification, the spot size is of the order of a few microns. All the measurements were performed in air.

EUV transient-grating

The EUV gratings were generated at the EIS-TIMER beamline^{15,38,39} using the radiation generated by the double stage FEL source (FEL2) available at the FERMI free-electron laser radiation⁴⁰. Fig. 1(c) illustrates the EUV TG experimental geometry. Two symmetric pump beams with wavelength $\lambda_{pu} = 39.9$ nm and time duration < 100 fs, generated by the first stage of the FEL, are crossed at the sample with an angle $2\theta=27.6^\circ$ generating a TG with a periodicity $\Pi = 2\pi/k_{TG}=83.6$ nm, where $k_{TG} = 4\pi\sin(\theta)/\lambda_{pu} = 0.075$ nm⁻¹ is the modulus of the TG vector. As a probe, we used the output of the second stage of the FEL, which was set at $\lambda_{pr} = 13.3$ nm.

The spot sizes, full width at half maximum (FWHM), of the two pump beams were (380x290) μm^2 and (470x250) μm^2 . The probe

beam at the sample had a spot size of (450x330) μm^2 . Unlike a typical pump-probe experiment, in a TG measurement the recorded signal originates only from the probe beam fraction which is diffracted by the transient grating. Thus, it only results from the region where the three beams are superimposed. All the measurements were performed in reflection geometry, in high vacuum and at room temperature. The diffracted signal was recorded using a CCD camera. The fluence values reported in the text refer to the sum of the incident fluences of the two pumps, whose pulse energies are approximately equal. The FEL intensity at the sample was varied by using a nitrogen gas cell, which efficiently attenuates the radiation at λ_{pu} while it marginally affects the transmission of the probe beam. Typically, the acquisition of the EUV-TG signal takes about 1-2 minutes per delay point, leading to 1-2 hours for a full trace and a good signal-to-noise ratio. An estimate of the uncertainty over the TG signal values at EIS-TIMER beamline was discussed by Benicivenga et al.¹⁵. The spatial and temporal overlap between the two pump and the probe beams were checked separately using a reference IR laser and performing FEL-pump/IR-probe transient transmissivity experiments on a YAG reference sample.

The attenuation lengths for the incident FEL pumps in MoS₂ and Si can be derived from the tabulated atomic data found in Henke et al.⁴¹. We obtain ≈ 40 nm and ≈ 237 nm, respectively, while these values are ≈ 205 nm and ≈ 583 nm at $\lambda_{pr} = 13.3$ nm. An extended wavelength dependence and comparison with other common substrates for MoS₂ can be found in the Supplemental Material¹⁷.

Acknowledgement

A.M. and C.G. acknowledge financial support from MIUR through the PRIN 2015

(Prot. 2015C5SEJJ001) and PRIN 2017 (Prot. 20172H2SC4_005) programs and from the European Union - Next Generation EU through the MUR-PRIN2022 (Prot. 20228YCY7) program.

C.G. acknowledges support from Università Cattolica del Sacro Cuore through D.1, D.2.2 and D.3.1 grants.

Sample fabrication of sample #2 was supported by the Columbia Nano Initiative and Columbia Materials Science and Engineering Research Center (MRSEC) through NSF grant DMR-2011738.

P.M and S.U. acknowledge funding from the Danish Council for Independent Research, Natural Sciences under the Sapere Aude program (Grant No. DFF- 9064-00057B), VILLUM FONDEN under the Centre of Excellence for Dirac Materials (grant 11744), and from the Novo Nordisk Foundation (Project Grant NNF22OC0079960).

Supplementary Information on Impact of a MoS₂ monolayer on the nanoscale thermoelastic response of silicon heterostructures

Micro-Raman characterization

In the main text, selected scans of the micro-Raman characterization for the Stokes scattering signal were reported in Fig. 1(b). The spectral window was centered around two peaks corresponding to the E_{2g}^1 and A_{1g} near-zone center phonon modes of the MoS₂ film with frequencies at $\approx 385 \text{ cm}^{-1}$ and $\approx 404 \text{ cm}^{-1}$ respectively. In Fig. S1 we report, measured at the same sample positions, the peaks corresponding to the (degenerate) optical phonon mode of Si at $\approx 520 \text{ cm}^{-1}$. For sample #3, however, the Si line was saturating the detector and thus it was acquired in a separate scan with the incident power reduced by a factor 10. The Raman frequency and narrow linewidth of the Si phonon peak from the substrates confirm a single-crystal structure^{42,43}.

To test the uniformity of the MoS₂ film coverage for samples #2 and #3, we performed a 5x5 raster scan, *i.e.*, a series of consecutive Raman spectra taken along a regular grid.

In Fig. S2, we show the 5x5 raster scan scheme employed for the micro-Raman measurements. Panel (a) shows the coordinates of the employed grid (in μm), superimposed to sample #2 in panel (b). An equivalent pattern was used to characterize samples #1, #3 and a blank Si wafer. The spectra were fitted using a series of Voigt peaks, one for each Raman resonance on top of a quadratic background. The point by point results for the peak frequencies of the two MoS₂ Raman-active modes E_{2g}^1 and A_{1g} and their separation are shown in Fig. S3. In both sample #2 and #3, we observe an overall uniform coverage with the values matching those of a monolayer film¹.

A picture of the multilayer, bulk-like, region found on the Si frame of sample #2 is reported in Fig. S4. On such island we acquired the ‘bulk island’ traces from Fig. 1(b) and S1.

The average frequency (f) and FWHM (w) of the MoS₂ and Si peaks for the studied samples are summarized in Tables 1, 2, together with the spectral separation of the MoS₂ peaks (Δ).

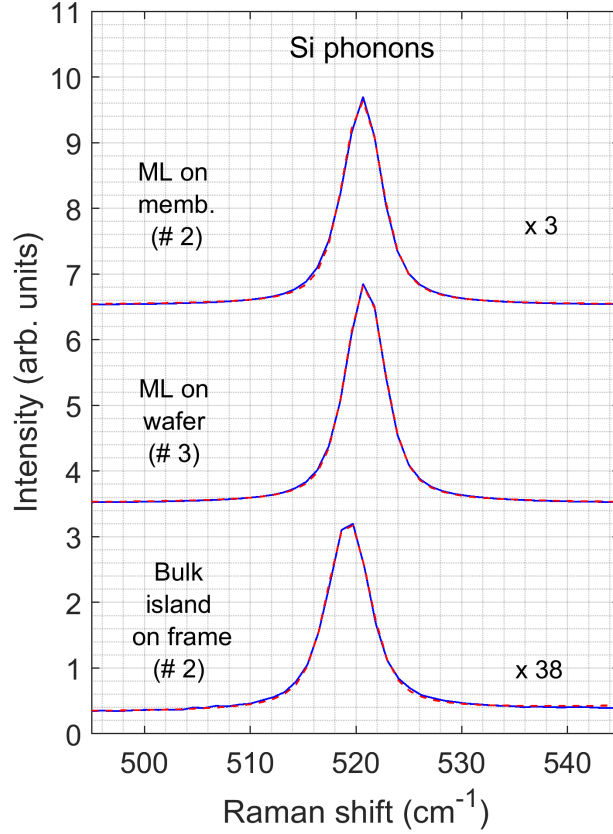


FIG. S1. Selected micro-Raman spectra showing the Si optical phonon peak from the investigated samples (MoS₂/Si membrane, MoS₂/Si wafer and a MoS₂ bulk island). The Raman traces were rescaled and vertically shifted for clarity. The blue lines correspond to the experimental data, while the red-dotted ones to the best fit to a Voigt peak on top of a quadratic background.

Table 1: Micro-Raman characterization results for regions with MoS₂ film. All the numerical results are expressed in cm⁻¹. The abbreviation ‘m.’, ‘i.’ and ‘w.’ stand for ‘membrane’, ‘island’ and ‘wafer’ respectively.

| Sample | $f_{E_{2g}^1}$ | $w_{E_{2g}^1}$ | $f_{A_{1g}}$ | $w_{A_{1g}}$ | $\Delta_{A_{1g}-E_{2g}^1}$ | f_{Si} | w_{Si} |
|-------------------------|-------------------|-----------------|-------------------|-----------------|----------------------------|-------------------|-----------------|
| MoS ₂ /Si m. | 384.6 ± 0.1 | 4.02 ± 0.08 | 404.2 ± 0.2 | 6.0 ± 0.1 | 19.7 ± 0.3 | 519.97 ± 0.08 | 4.61 ± 0.03 |
| MoS ₂ /Si i. | 381.83 ± 0.04 | 3.83 ± 0.07 | 407.03 ± 0.02 | 4.57 ± 0.04 | 25.20 ± 0.05 | 519.29 ± 0.01 | 4.94 ± 0.02 |
| MoS ₂ /Si w. | 385.4 ± 0.1 | 4.26 ± 0.04 | 404.4 ± 0.2 | 6.4 ± 0.2 | 18.9 ± 0.4 | 520.91 ± 0.04 | 4.55 ± 0.05 |

Table 2: Micro-Raman characterization results for the filmless substrates. All the numerical results are expressed in cm⁻¹.

| Sample | f_{Si} | w_{Si} |
|-------------|-------------------|-----------------|
| Si membrane | 520.5 ± 0.1 | 4.32 ± 0.04 |
| Si wafer | 520.98 ± 0.06 | 4.63 ± 0.04 |

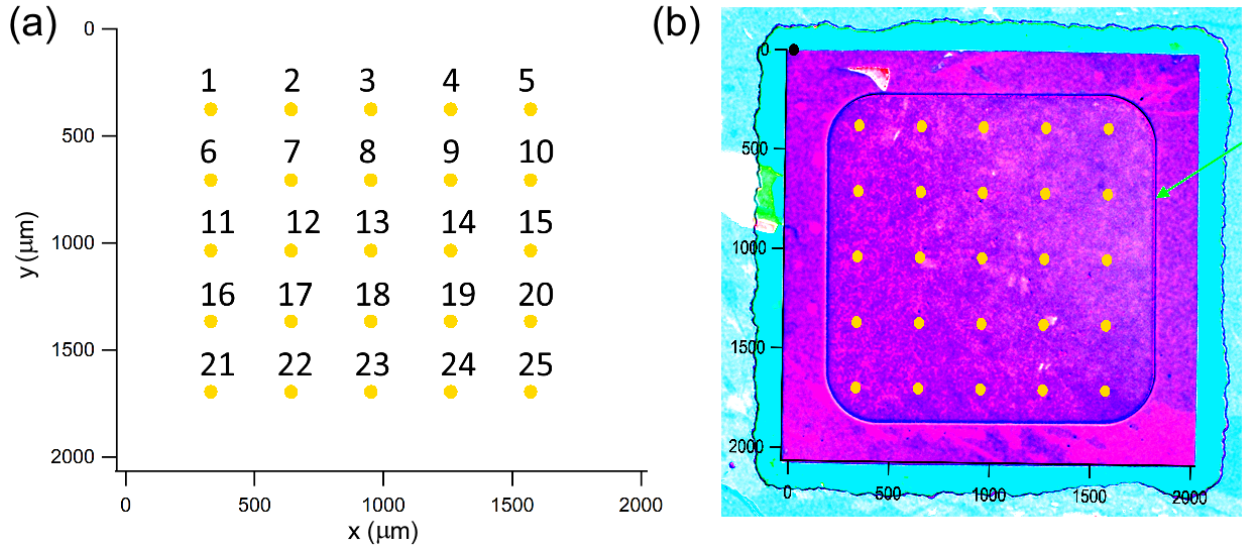


FIG. S2. (a) Scheme for the raster scan pattern to test the uniformity of the MoS₂ on the silicon substrate. The axes are in micrometers. (b) Optical-microscope picture of sample #2 after changing the tonality and saturation levels to emphasize the macroscopic morphology of the film. The light blue section corresponds to the frame, while the pink regions to the membrane. The membrane border is indicated by the green arrow.

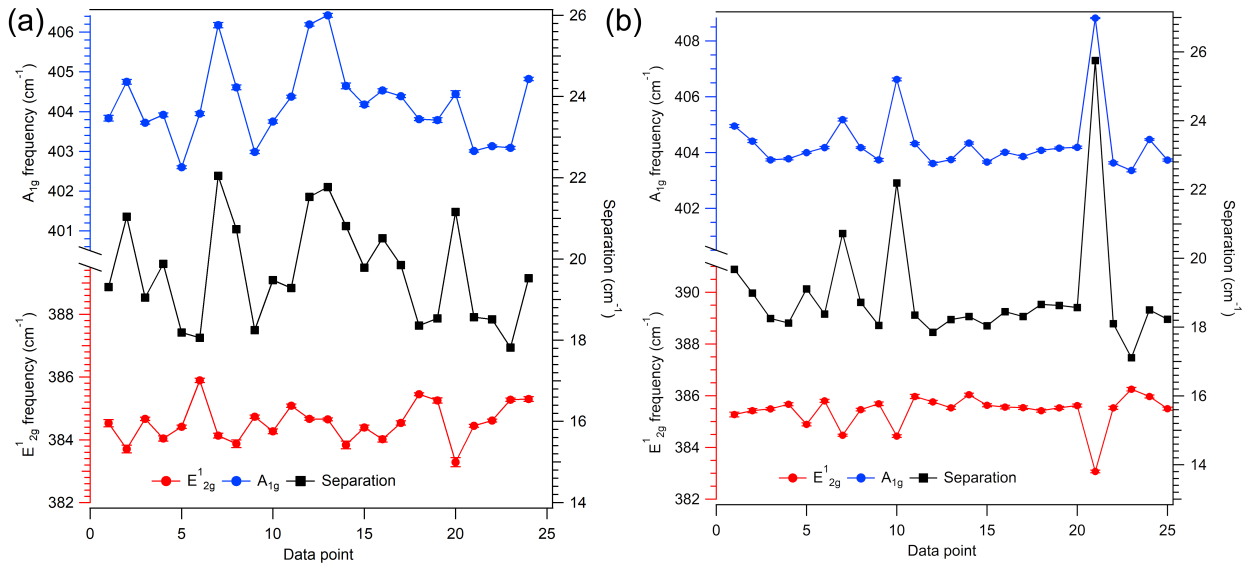


FIG. S3. The left vertical scale refers to the peak positions for the E_{2g}^1 and A_{1g} MoS₂ modes acquired at the positions of the raster scans (Fig. S2) through micro-Raman measurements, while the right vertical scale refers to the spectral separation between the two peaks; the linewidth of the Raman peaks was about 4 cm⁻¹. (a) Sample #2 (b) Sample # 3.

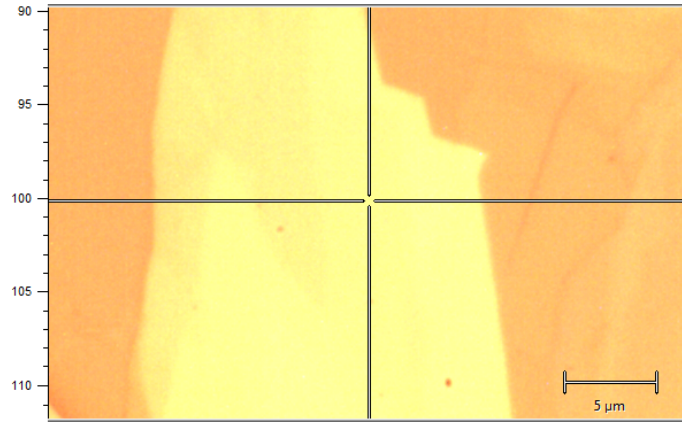


FIG. S4. Multilayer, showing bulk-like response, MoS₂ region found on the Si frame of sample #2.

EUV/ Soft x-ray beam attenuation length

The EUV / Soft x-ray wavelength dependence of the attenuation length for different materials is reported in Fig. S5. As shown by the logarithmic plot, Si is the most transparent one under the wavelengths used in our transient grating FEL experiments (13.3-39.9 nm). At $\lambda_{pu}=39.9$ nm, its attenuation length is about one order of magnitude larger than the others, which indicates that the pump beams travel through the whole Si membrane used for the MoS₂/Si membrane sample (≈ 237 nm) without severe energy reduction. A different case is, e.g., sapphire for which the attenuation length is ≈ 13 nm, therefore meaning that a transient grating generated by 39.9 nm beams will be localized close to the surface and leading to a much higher energy density under the same excitation conditions.

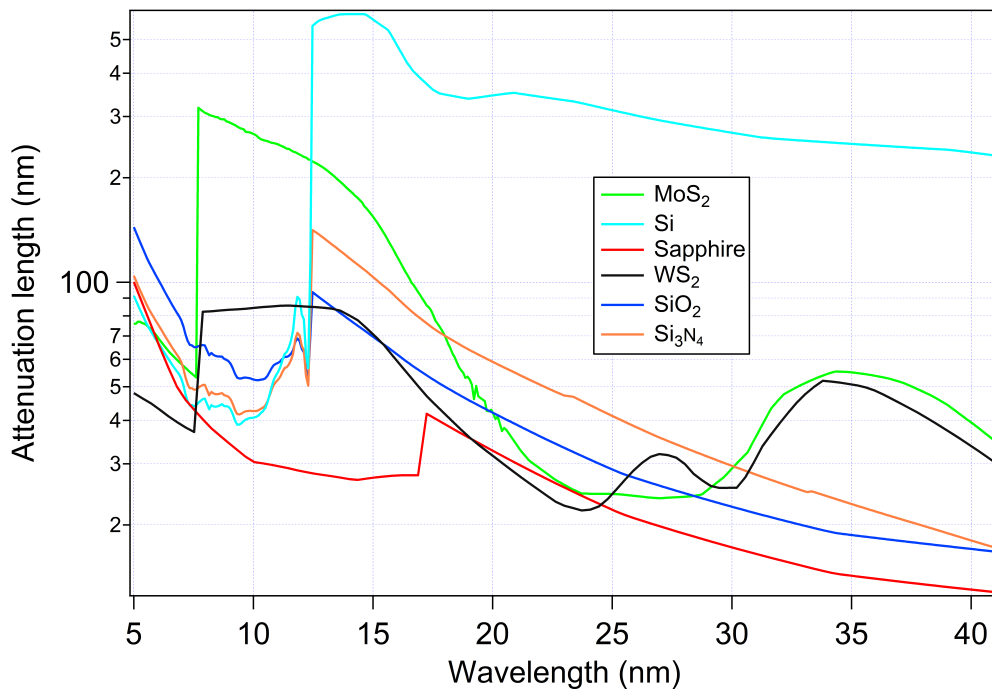


FIG. S5. EUV / Soft x-ray attenuation lengths for different materials. The curves were calculated using the scattering factor data from⁴¹.

Additional TG results

MoS₂/Si wafer TG at different points

We report in Fig. S6 the TG response collected on the MoS₂/Si wafer at different positions on the sample. While we observed some variability in the amplitude and decay time of the non-oscillating signal in the recorded window, possibly due to the local morphology of both the substrate and the film, the double peak structure and the general characteristics of the response are maintained.

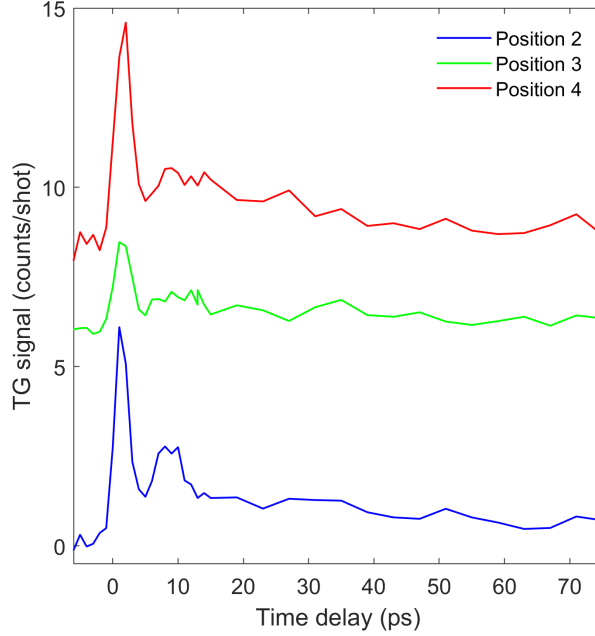


FIG. S6. TG signal from the MoS₂/Si wafer sample taken at different positions from the dataset of Fig. 4(a) at ≈ 0.3 mJ/cm² fluence.

Silicon frame

As a comparison, we show in Fig. S7 the TG signal obtained from the 200- μ m-thick supporting frame of the silicon membrane. While its bulk is still made of silicon, the surface is covered by a thin oxide layer for surface protection purposes.

Compared to the blank membrane response (Fig. 2(a)), the oscillatory response displays a slower decay.

WS₂/Sapphire

Fig. S8 shows in the EUV TG signal of a different heterostructure, a CVD-grown monolayer WS₂ on a ≈ 0.5 -mm *c*-cut sapphire substrate (commercially available from 2D Semiconductors), collected at different grating periods, obtained by changing λ_{pu} from (a) 39.9 nm ($L_{TG}=83.6$ nm) to (b) 26.6 nm ($L_{TG}=55.8$ nm) or (c) 13.3 nm ($L_{TG}=27.9$ nm). Differently from the MoS₂/Si samples examined in the main text, here we notice that a single oscillatory term in Eq. 1 is enough to describe the TG response. In panel (d) we show the obtained frequencies as a function of the transient grating wavevector. Although collected at different fluences, we assume the acoustic wave propagation velocities to be almost independent from it, similarly to the MoS₂/Si wafer data in Fig. 4(a). Through a linear fit, fixing the intercept to 0, we obtain an estimate propagation speed $v=(5.398 \pm 0.009)$ km/s. This is in good agreement with the Rayleigh mode of sapphire, reported to have a velocity ≈ 5.4 km/s⁴⁴. Correspondingly, we have for the non-oscillating background decay constant τ_{th} the following fit results: (a) (38 ± 2) ps (b) (35 ± 2) ps (c) (11 ± 3) ps. The last value is, however, affected by the poorer

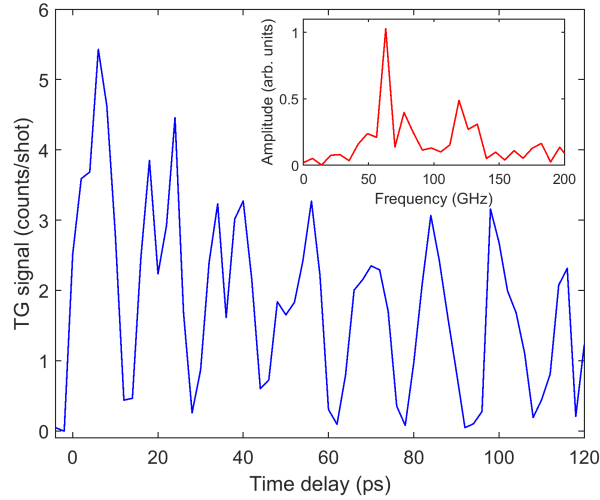


FIG. S7. Transient grating signal acquired on the Si frame of the blank Si membrane sample using a 83.6 nm grating period acquired under 0.2 mJ/cm² incident fluence respectively. The inset show the discrete Fourier transform of the TG signal.

TG signal signal-to-noise ratio connected to the 13.3 nm pump - 13.3 probe signal, since this configuration is limited by the impossibility to freely vary the relative fluence for pump and probe. While in the second part of the explored time delay range (especially visible in panels (a) and (b)), we observe a second harmonic modulation, connected to the square in Eq. 2, the main frequency dominates elsewhere with a possible contribution of the longitudinal-like mode the first tens of picoseconds, similarly to the samples studied in the main text. The longitudinal speed in sapphire is expected to be ≈ 11 km/s⁴⁵, corresponding to frequencies of (a) ≈ 132 GHz (b) ≈ 198 GHz (c) ≈ 395 GHz. The reason why the Rayleigh mode for this sample dominates the response even in the presence of the WS₂ film is likely connected to the much shallower penetration of the pump beams in sapphire (Fig. S5) compared to Si, leading to a significantly higher energy density near the surface, *i.e.* where the surface acoustic waves such as the Rayleigh mode are localized. Moreover, as we saw in Fig. 4(a) for the MoS₂ / Si wafer sample, higher excitation fluences could favor the emergence of the Rayleigh mode in the TG signal in WS₂/Sapphire due to larger initial displacements.

Acoustic waves schemes

In Figs. S9 and S10 we report simulations of the propagation of the longitudinal and Rayleigh mode on a semi-infinite bulk Si substrate at different time delays within an oscillation period. The plots were drawn using a regular 75 x 75 rectangular point grid. The (relative) displacements were calculated based on the derivation reported in Royer and Valier-Brasier using the method of potentials in the isotopic approximation (Chapter 1 and 3)¹⁹. The displacements \vec{u} were considered at different positions x parallel to the surface and depths with respect to the surface ($y = 0$, positive values for larger depths in Si). For the longitudinal mode propagating parallel to the surface, we used a simple sinusoidal form

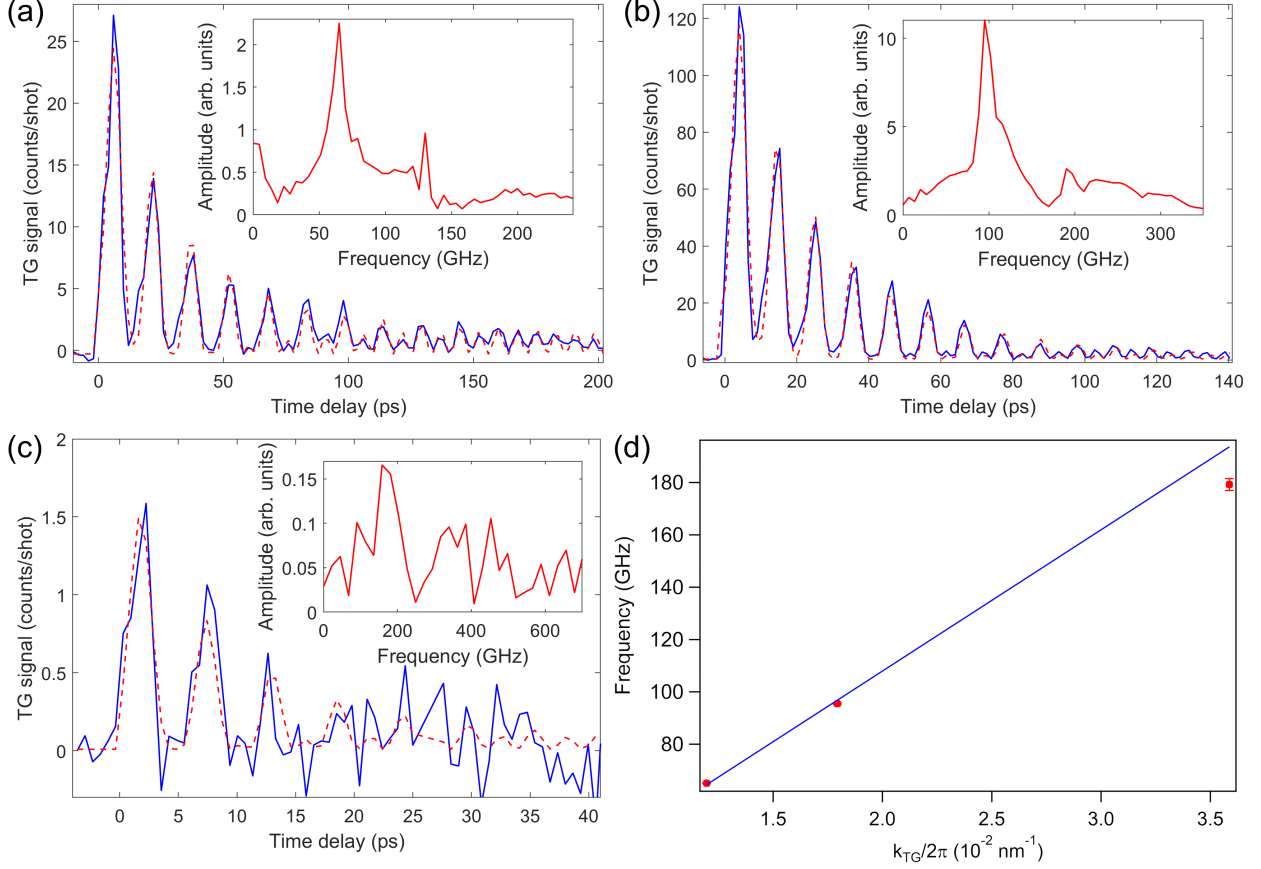


FIG. S8. TG signal for $\text{WS}_2/\text{Sapphire}$ using different transient grating periods. (a) 84 nm under 0.1 mJ/cm^2 (b) 56 nm under 0.7 mJ/cm^2 (c) 28 nm under $<0.1 \text{ mJ/cm}^2$ (exact estimation not accurately available). (d) Frequency of the Rayleigh mode as a function of the transient grating wavevector k_{TG} . The experimental data is represented by blue traces, the fit curves by dotted red lines.

$$\begin{cases} u_x(x, y) = U \cos(k_{TG}x - \omega t) \\ u_y(x, y) = 0 \end{cases} \quad (2)$$

where U is the amplitude of the mode, k_{TG} the wavevector and ω is the angular frequency. In order to make the shifts visible, we set the amplitude to an arbitrary value. In the plot, the color scale is normalized by the largest magnitude among the calculated displacements.

Regarding the Rayleigh wave, the displacements are

$$\begin{cases} \text{Re}[u_x(x, y)] = U_1(y) \sin(k_{TG}x - \omega t) \\ \text{Re}[u_y(x, y)] = U_2(y) \cos(k_{TG}x - \omega t) \end{cases} \quad (3)$$

where $\omega = k_{TG}v_R$ with v_R Rayleigh velocity and the amplitudes

$$\begin{cases} U_1(y) = a_L [-k_{TG}e^{-\alpha_L y} + \sqrt{\alpha_L \alpha_T} e^{-\alpha_T y}] \\ U_2(y) = a_L \sqrt{\frac{\alpha_L}{\alpha_T}} [-\sqrt{\alpha_L \alpha_T} e^{-\alpha_L y} + k_{TG} e^{-\alpha_T y}] \end{cases} \quad (4)$$

where a_L is the longitudinal amplitude (connected to the transverse one via $a_T = i\sqrt{\frac{\alpha_L}{\alpha_T}}a_L$), $\alpha_i = \sqrt{k_{TG}^2 - k_i^2}$ is a constant with $k_i = \omega/v_i$ connected to the velocity v_i with $i = l, t$ differentiating longitudinal and transverse parameters respectively. The longitudinal, transverse velocities and Rayleigh values were taken from Farnell and Adler²¹. To ease visibility, the amplitude a_L was set to an arbitrary value.

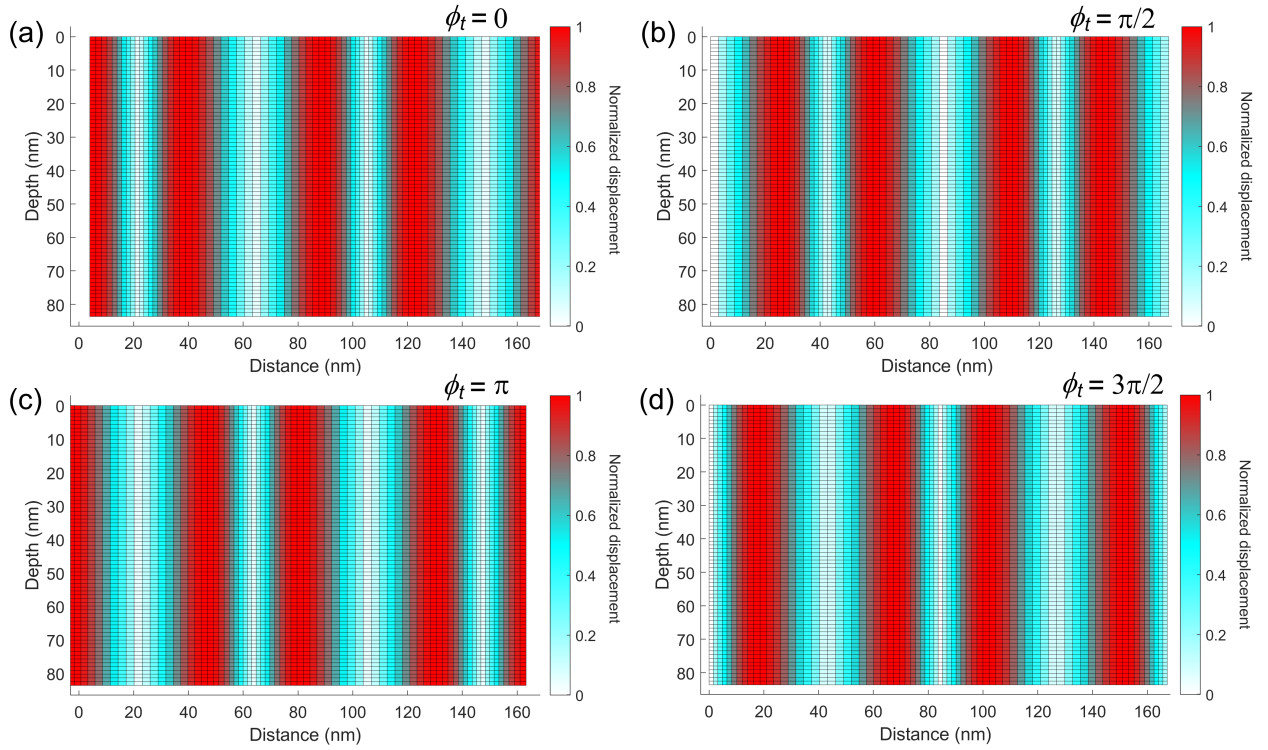


FIG. S9. Schemes of the displacements connected to a longitudinal wave in Si at four different time instants, expressed as $\phi_t = \omega t$.

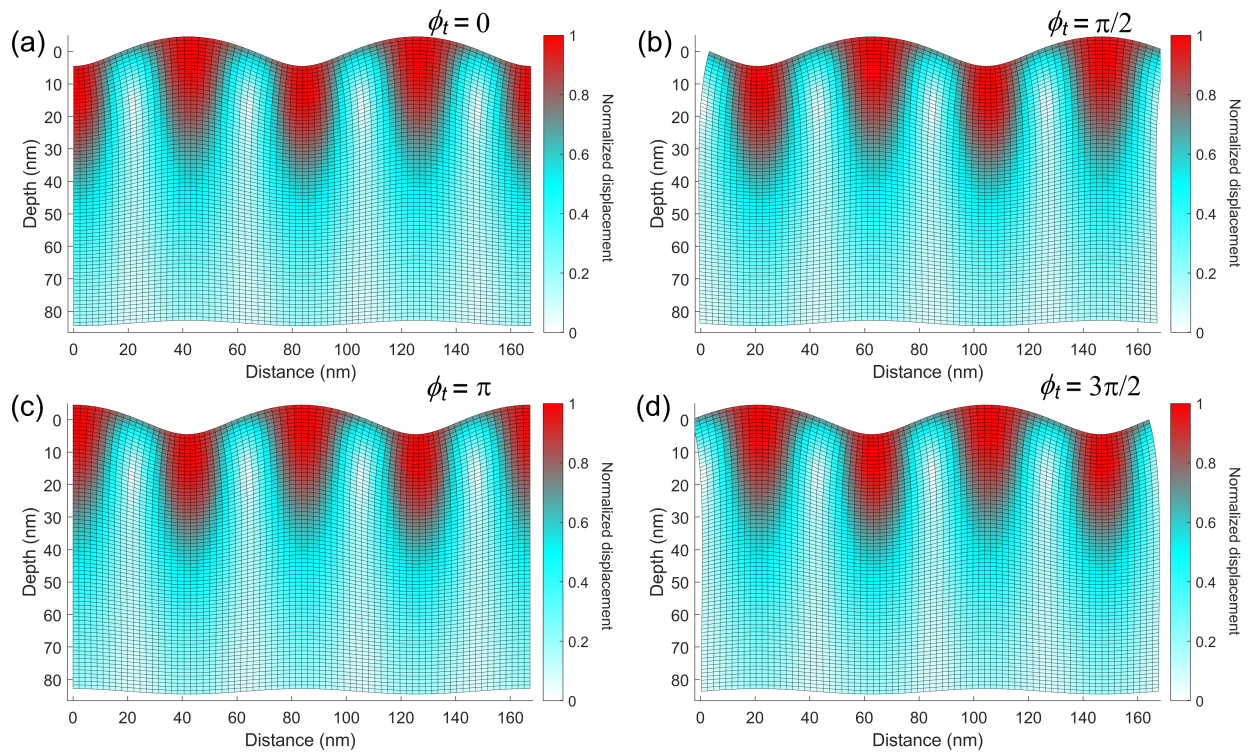


FIG. S10. Schemes of the displacements connected to a Rayleigh wave in Si at four different time instants, expressed as $\phi_t = \omega t$.

References

- (1) Lee, C.; Yan, H.; Brus, L. E.; Heinz, T. F.; Hone, J.; Ryu, S. Anomalous Lattice Vibrations of Single- and Few-Layer MoS₂. *ACS Nano* **2010**, *4*, 2695–2700.
- (2) Wang, Q. H.; Kalantar-Zadeh, K.; Kis, A.; Coleman, J. N.; Strano, M. S. Electronics and optoelectronics of two-dimensional transition metal dichalcogenides. *Nature Nanotechnology* **2012**, *7*, 699–712.
- (3) Golovynskyi, S.; Irfan, I.; Bosi, M.; Seravalli, L.; Datsenko, O. I.; Golovynska, I.; Li, B.; Lin, D.; Qu, J. Exciton and trion in few-layer MoS₂: Thickness- and temperature-dependent photoluminescence. *Applied Surface Science* **2020**, *515*, 146033.
- (4) Ellis, J. K.; Lucero, M. J.; Scuseria, G. E. The indirect to direct band gap transition in multilayered MoS₂ as predicted by screened hybrid density functional theory. *Applied Physics Letters* **2011**, *99*, 261908.
- (5) Gabourie, A. J.; K orođlu, c. C.; Pop, E. Substrate-dependence of monolayer MoS₂ thermal conductivity and thermal boundary conductance. *Journal of Applied Physics* **2022**, *131*, 195103.
- (6) Li, G.; Chen, Z.; Li, Y.; Zhang, D.; Yang, W.; Liu, Y.; Cao, L. Engineering Substrate Interaction To Improve Hydrogen Evolution Catalysis of Monolayer MoS₂ Films beyond Pt. *ACS Nano* **2020**, *14*, 1707–1714.
- (7) Agmon, L.; Almog, R.; Gaspar, D.; Vosco-boynik, G.; Choudhary, M.; Jopp, J.; Klausner, Z.; Ya’akobovitz, A.; Berkovich, R. Nanoscale contact mechanics of the interactions at monolayer MoS₂ interfaces with Au and Si. *Tribology International* **2022**, *174*, 107734.
- (8) Kuppadakkath, A. et al. Direct growth of monolayer MoS₂ on nanostructured silicon waveguides. *Nanophotonics* **2022**, *11*, 4397–4408.
- (9) Hartmann, C. S. Systems Impact of Modern Rayleigh Wave Technology. Rayleigh-Wave Theory and Application. Berlin, Heidelberg, 1985; pp 238–253.
- (10) Biryukov, S. V.; Gulyaev, Y. V.; Krylov, V. V.; Plessky, V. P. *Surface Acoustic Waves in Inhomogeneous Media*; Springer-Verlag Berlin Heidelberg, 1995.
- (11) Bergin, S. M.; Chen, Y.-H.; Rathmell, A. R.; Charbonneau, P.; Li, Z.-Y.; Wiley, B. J. The effect of nanowire length and diameter on the properties of transparent, conducting nanowire films. *Nanoscale* **2012**, *4*, 1996–2004.
- (12) Leong, W. S.; Luo, X.; Li, Y.; Khoo, K. H.; Quek, S. Y.; Thong, J. T. L. Low Resistance Metal Contacts to MoS₂ Devices with Nickel-Etched-Graphene Electrodes. *ACS Nano* **2015**, *9*, 869–877.
- (13) Ganatra, R.; Zhang, Q. Few-Layer MoS₂: A Promising Layered Semiconductor. *ACS Nano* **2014**, *8*, 4074–4099.

- (14) Nelson, K. A.; Miller, R. J. D.; Lutz, D. R.; Fayer, M. D. Optical generation of tunable ultrasonic waves. *Journal of Applied Physics* **1982**, *53*, 1144–1149.
- (15) Bencivenga, F. et al. Nanoscale transient gratings excited and probed by extreme ultraviolet femtosecond pulses. *Science Advances* **2019**, *5*, 7, eaaw5805.
- (16) Liu, F.; Wu, W.; Bai, Y.; Chae, S. H.; Li, Q.; Wang, J.; Hone, J.; Zhu, X.-Y. Disassembling 2D van der Waals crystals into macroscopic monolayers and reassembling into artificial lattices. *Science* **2020**, *367*, 903–906.
- (17) Soranzio, D. Supplementary information. 2024.
- (18) Auld, B. A. *Acoustic fields and waves in solids. Vol. 2*; John Wiley I& Sons, New York, 1973.
- (19) Royer, D.; Valier-Brasier, T. *Elastic Waves in Solids 1: Propagation*; ISTE, London and John Wiley & Sons, New York, 2022.
- (20) Milloch, A. Nanoscale thermoelasticity in mechanically confined systems. M.Sc. thesis, Università degli studi di Trieste, 2020.
- (21) Farnell, G.; Adler, E. *Elastic Wave Propagation in Thin Layers*; Physical Acoustics; Academic Press, 1972; Vol. 9; pp 35–127.
- (22) Janušonis, J.; Jansma, T.; Chang, C. L.; Liu, Q.; Gatilova, A.; Lomonosov, A. M.; Shalagatskyi, V.; Pezeril, T.; Temnov, V. V.; Tobey, R. I. Transient Grating Spectroscopy in Magnetic Thin Films: Simultaneous Detection of Elastic and Magnetic Dynamics. *Scientific Reports* **2016**, *6*, 29143.
- (23) Maznev, A. A. et al. Generation of coherent phonons by coherent extreme ultraviolet radiation in a transient grating experiment. *Applied Physics Letters* **2018**, *113*, 221905.
- (24) Brioschi, M.; Carrara, P.; Polewczyk, V.; Dagur, D.; Vinai, G.; Parisse, P.; Zilio, S. D.; Panaccione, G.; Rossi, G.; Cucini, R. Multidetector scheme for transient-grating-based spectroscopy. *Opt. Lett.* **2023**, *48*, 167–170.
- (25) Foglia, L. et al. Extreme ultraviolet transient gratings: A tool for nanoscale photoacoustics. *Photoacoustics* **2023**, *29*, 100453.
- (26) Bencivenga, F.; Capotondi, F.; Foglia, L.; Mincigrucci, R.; Masciovecchio, C. Extreme ultraviolet transient gratings. *Advances in Physics: X* **2023**, *8*, 2220363.
- (27) Janušonis, J.; Chang, C. L.; Jansma, T.; Gatilova, A.; Vlasov, V. S.; Lomonosov, A. M.; Temnov, V. V.; Tobey, R. I. Ultrafast magnetoelastic probing of surface acoustic transients. *Phys. Rev. B* **2016**, *94*, 024415.
- (28) Xu, B.; Shen, Z.; Ni, X.; Lu, J. Numerical simulation of laser-generated ultrasound by the finite element method. *Journal of Applied Physics* **2004**, *95*, 2116–2122.

- (29) Veres, I. A.; Berer, T.; Burgholzer, P. Numerical modeling of thermoelastic generation of ultrasound by laser irradiation in the coupled thermoelasticity. *Ultrasonics* **2013**, *53*, 141–149.
- (30) Liu, Z.; Lin, B.; Liang, X.; Du, A. Numerical simulation of laser-generated Rayleigh wave pulses propagation in the machined surface with residual stress using finite-difference method. *Optik* **2021**, *248*, 168072.
- (31) Wang, J.; Wu, S.; Xie, H.; Xiong, L. Theoretical study on thermal properties of molybdenum disulfide/silicon heterostructures. *Computational Materials Science* **2021**, *200*, 110835.
- (32) Liu, W.; Huang, X.; Yue, Y. Tuning thermal transport across monolayer MoS₂/Si heterostructure via substrate nanogrooving. *International Journal of Heat and Mass Transfer* **2023**, *201*, 123673.
- (33) Johnson, J. A.; Maznev, A. A.; Cuffe, J.; Eliason, J. K.; Minnich, A. J.; Kehoe, T.; Torres, C. M. S.; Chen, G.; Nelson, K. A. Direct Measurement of Room-Temperature Nondiffusive Thermal Transport Over Micron Distances in a Silicon Membrane. *Phys. Rev. Lett.* **2013**, *110*, 025901.
- (34) Maznev, A. A.; Johnson, J. A.; Nelson, K. A. Onset of nondiffusive phonon transport in transient thermal grating decay. *Phys. Rev. B* **2011**, *84*, 195206.
- (35) Zhao, Y.; Ouyang, G. Thickness-dependent photoelectric properties of MoS₂/Si heterostructure solar cells. *Scientific Reports* **2019**, *9*, 17381.
- (36) Vialla, F.; Fatti, N. D. Time-Domain Investigations of Coherent Phonons in van der Waals Thin Films. *Nanomaterials* **2020**, *10*, *12*, 2543.
- (37) Norcada: a MEMS technology company. <https://www.norcada.com/>, Accessed: 2023-11-07.
- (38) Mincigrucci, R. et al. Advances in instrumentation for FEL-based four-wave-mixing experiments. *Nuclear Instruments and Methods in Physics Research Section A: Accelerators, Spectrometers, Detectors and Associated Equipment* **2018**, *907*, 132–148, Advances in Instrumentation and Experimental Methods (Special Issue in Honour of Kai Siegbahn).
- (39) Bencivenga, F. et al. Four-wave mixing experiments with extreme ultraviolet transient gratings. *Nature* **2015**, *520*, 205–208.
- (40) Allaria, E. et al. Two-stage seeded soft-X-ray free-electron laser. *Nature Photonics* **2013**, *7*, 913–918.
- (41) Henke, B.; Gullikson, E.; Davis, J. X-Ray Interactions: Photoabsorption, Scattering, Transmission, and Reflection at E = 50–30,000 eV, Z = 1–92. *Atomic Data and Nuclear Data Tables* **1993**, *54*, 181–342.

- (42) Lambertz, A.; Richards, B.; Sproul, A.; Puzzer, T.; Gross, M. Sputter Deposited and Solid Phase Crystallized Silicon Films for Solar Cells. Proceedings of the 2nd World Conference on Photovoltaic Solar Energy Conversion. 1998; p 1294.
- (43) Yeh, W. Fabrication of single crystalline stripe in Si and Ge film on rolled flexible glass substrate by UV cw micro-chevron laser beam. Low-Dimensional Materials and Devices 2017. 2017; pp 31 – 37.
- (44) Pedrós, J.; Calle, F.; Grajal, J.; Jiménez Riobóo, R.; Prieto, C.; Pau, J.; Pereiro, J.; Hermann, M.; Eickhoff, M.; Bougrioua, Z. Anisotropic propagation of surface acoustic waves on nitride layers. *Superlattices and Microstructures* **2004**, *36*, 815–823, European Materials Research Society 2004, Symposium L. InN, GaN, AlN and Related Materials, their Heterostructures and Devices.
- (45) Winey, J. M.; Gupta, Y. M.; Hare, D. E. r-axis sound speed and elastic properties of sapphire single crystals. *Journal of Applied Physics* **2001**, *90*, 3109–3111.